IMAGE RECONSTRUCTION

Computed tomography (*CT*) is an imaging technique that has revolutionized the field of medical diagnostics. *CT* has also found applications in many other areas such as nondestructive evaluation of industrial and biological specimens, radioastronomy, light and electron microscopy, optical interferometry, X-ray crystallography, petroleum engineering, and geophysical exploration. Indirectly, it has also led to new developments in its predecessor techniques in radiographic imaging.

The fundamental principle behind CT, namely, image reconstruction from projections, has been known for about 80 years, since the exposition of the topic by Radon (1) in 1917. More recent developments in the subject arose in the 1950s and 1960s from work by a number of researchers in diverse applications. Some important publications in this area are those by Cormack (2, 3) on the representation of a function by its line integrals; by Bracewell and Riddle (4) on the reconstruction of brightness distributions of astronomical bodies from fan-beam scans at various angles; by 5, 6) on the reconstruction of three-dimensional (3-D) images of viruses from electron micrographs; by 7 on the convolution backprojection technique; and by Gordon et al. (8) on algebraic reconstruction techniques. Pioneering work on the development of practical scanners for medical applications was done by 9, 10, and 11. X-ray CT was well established as a clinical diagnostic tool by the early 1970s.

Mathematically, the main principle behind *CT* imaging is that of estimating an image (object) from its projections (integrals) measured in different directions (1213141516171819–20). A projection of an image is also referred to as the Radon transform of the image at the corresponding angle, after the main proponent of the associated mathematical principles. In continuous space, the projections are ray integrals of the image, measured at different ray positions and angles; in practice, only discrete measurements are available. The solution to the problem of image reconstruction may be formulated variously as backprojecting and summing the given projection data, completing the corresponding Fourier space, solving a set of simultaneous equations, and so on. Each of these methods has its own advantages and disadvantages that determine its suitability to a particular imaging application.

In this article, we describe the three basic approaches to image reconstruction from projections mentioned above. Techniques for gathering the projection data as well as for display and processing of the reconstructed images in a few specific application areas will be described briefly.

Projection Data Collection Methods

In ordinary radiography, a two-dimensional (2-D) shadow of a 3-D body is produced on film by irradiating the body with X-ray photons [see Fig. 1(a).]. Each ray of X-ray photons is attenuated by a factor depending on the integral of the linear attenuation coefficient along the path of the ray and produces a corresponding gray level at the point hit on the film or the detecting device used. Let N_i denote the number of X-ray photons incident upon the body being imaged within a specified time interval for a particular ray path. Let N_o be the
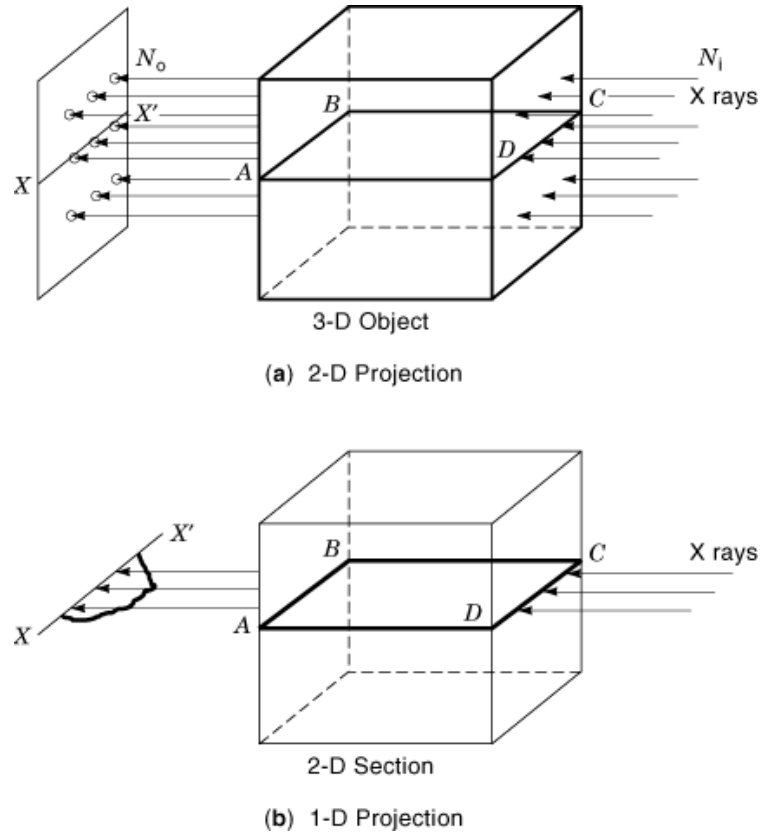
Fig. 1.   (a) An ordinary X-ray image or typical radiograph is a 2-D shadow of a 3-D object. The entire object is irradiated with X rays. (b) In *CT* imaging, only the desired sectional plane of the body—labeled as the plane *ABCD* in the figure—is irradiated. The measured data represent a 1-D projection of a 2-D cross-sectional plane of the object. The profile *X–X′* in (a) and the projection *X–X′* in (b) should be identical except for the effects of scattered radiation.

corresponding number of photons exiting the body. Then, we have

$$N_{\mathrm{o}} = N_{\mathrm{i}} \exp[-\int \mu(x, y)\, ds]$$

or

$$\int \mu(x, y)\, ds = \ln\left(\frac{N_{\mathrm{i}}}{N_{\mathrm{o}}}\right) \qquad (1)$$

N_{i} and N_{o} are Poisson variables; it is assumed that they are very large for the above equations to be applicable. $\mu(x, y)$ represents the linear attenuation coefficient at (x, y), ds represents the elemental distance along the ray, and the integral is along the ray path from the X-ray source to the detector. The value of $\mu(x, y)$ depends on the density of the object or its constituents along the ray path, as well as the frequency (or wavelength or energy) of the radiation used. Equation (1) assumes the use of monochromatic or monoenergetic X rays.

   A measurement of the exiting X rays (i.e., N_{o} and N_{i} for reference) thus gives us only an integral of $\mu(x, y)$ over the ray path. The internal details of the body along the ray path are compressed onto a single point on

the film or a single measurement. Extending the same argument to all ray paths, we see that the radiographic image so produced is a 2-D (X-ray) shadow of the 3-D object, where the internal details are superimposed.

The problem of obtaining details of the interior of the human body noninvasively had always been of interest, and within a few years after the discovery of X rays by Röntgen in 1895, techniques were developed to image sectional planes of the body. These methods, called laminagraphy, planigraphy, tomography, and so on (21), used synchronous movement of the X-ray source and film in such a way as to produce a sharp image of a single focal plane, with the images of all other planes being blurred; the methods had limited commercial success. *CT* imaging as we know it today was developed during the late 1960s and the early 1970s, producing images of cross sections of the human head and body as never seen before (noninvasively and nondestructively!). While the fundamental radiographical equation is the same as Eq. (1), in most *CT* scanners, only the desired cross section of the body is irradiated using a finely collimated ray of X-ray photons [see Fig. 1(b)], instead of irradiating the entire body with a solid beam of X rays as in ordinary radiography. Such ray integrals are measured at many positions and angles around the body, scanning the body in the process. The principle of image reconstruction from projections is then used to compute an image of a section of the body, hence the name *computed* tomography. [See 22 for an excellent review of the history of *CT* imaging; see also 23.]

Figure 2 depicts some of the scanning procedures employed: Figure 2(a) shows the translate–rotate scanning geometry for parallel-ray projections, Fig. 2(b) shows the translate-rotate scanning geometry with a small fan-beam detector array, Fig. 2(c) shows the rotate-only scanning geometry for fan-beam projections, and Fig. 2(d) shows the rotate-only scanning geometry for fan-beam projections using a ring of detectors. A more recently developed scanner specialized for cardiovascular imaging (24, 25) completely eliminates mechanical scanning movement to reduce scanning time by employing electronically steered X-ray microbeams and rings of detectors, as illustrated schematically in Fig. 3.

Once a sectional image is obtained, the process may be repeated to obtain a series of sectional images of the 3-D body or object being investigated. Imaging a 3-D body is usually accomplished by reconstructing one 2-D section at a time through the use of one-dimensional (1-D) projections. Exceptions to this are the Dynamic Spatial Reconstructor developed at the Mayo Clinic (22, 26), where a series of 2-D projection images are obtained via irradiation of the portion of the body of interest and a fluorescent screen, and single-photon emission computed tomography (*SPECT*), where a series of 2-D projection images are obtained using a gamma camera (17, 272829–30).

Some of the physical considerations in X-ray *CT* imaging are the effects of beam hardening, dual-energy imaging, scatter, photon detection noise, and ray stopping by heavy implants (18, 28, 29, 31).

- *Beam Hardening*. The X rays used in radiographic imaging are typically not monoenergetic; that is, they possess X-ray photons over a certain band of frequencies or electromagnetic energy levels. As the X rays propagate through a body, the lower-energy photons get absorbed preferentially (depending on the length of the ray path through the body and the attenuation characteristics of the material along the path). Thus the X rays that pass through the object at longer distances from the source will possess relatively fewer photons at lower-energy levels than at the point of entry into the object (and hence a relatively higher concentration of higher-energy photons). This effect is known as beam hardening. The effect of beam hardening may be reduced by prefiltering or prehardening the X-ray beam and narrowing its spectrum. Use of monoenergetic X rays from a synchrotron or a laser could also obviate this problem.
- *Dual-Energy Imaging*. Different materials have different energy-dependent X-ray attenuation coefficients. X-ray measurements or images obtained at multiple energy levels (also known as energy-selective imaging) could be combined to derive information about the distribution of specific materials in the object or body imaged. Weighted combinations of multiple energy images may be obtained to display soft-tissue and hard-tissue details separately (29).
- *Scatter*. As an X-ray beam propagates through a body, photons are lost due to absorption and scattering at each point in the body. The angle of the scattered photon at a given point along the incoming beam is
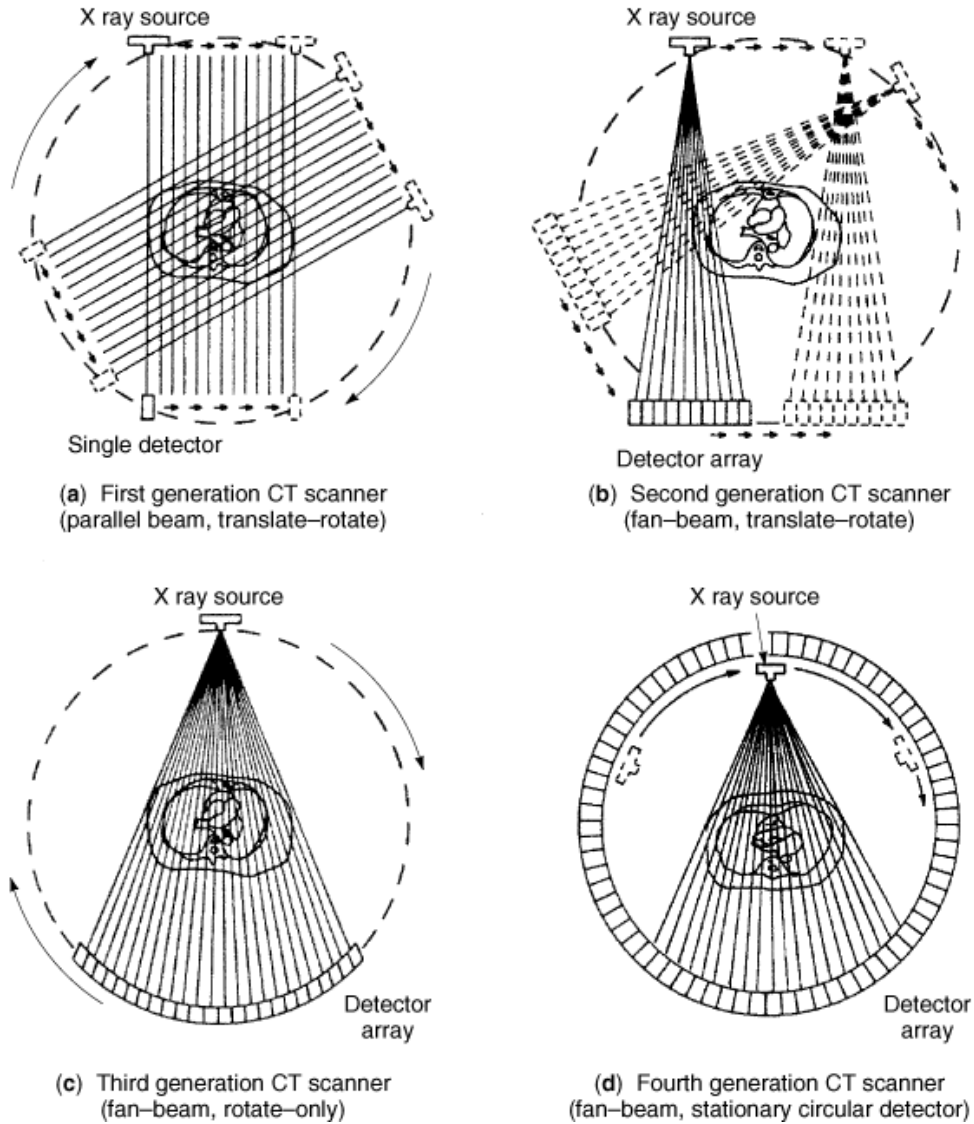
Fig. 2.   Translate–rotate scanning geometry for parallel-ray projections; (b) translate–rotate scanning geometry with a small fan-beam detector array; (c) rotate-only scanning geometry for fan-beam projections; and (d) rotate-only scanning geometry for fan-beam projections using a ring of detectors. (Reproduced with permission from R. A. Robb, X-ray computed tomography: An engineering synthesis of multiscientific principles, *CRC Crit. Rev. Biomed. Eng.*, **7**: 264–333, Mar. 1982. Copyright © 1982 CRC Press, Boca Raton, Florida.)

a random variable, and hence the scattered photon contributes to noise at the point where it strikes the detector. Furthermore, scattering results in loss of contrast of the part of the object where photons were scattered from the main beam. The noise effect of scattered radiation is significant in gamma-ray emission imaging (*SPECT*) and requires specific methods to improve the quality of the image (27, 28). The effect of scatter may be reduced by collimation or energy discrimination, as scattered photons usually have lower energy levels.
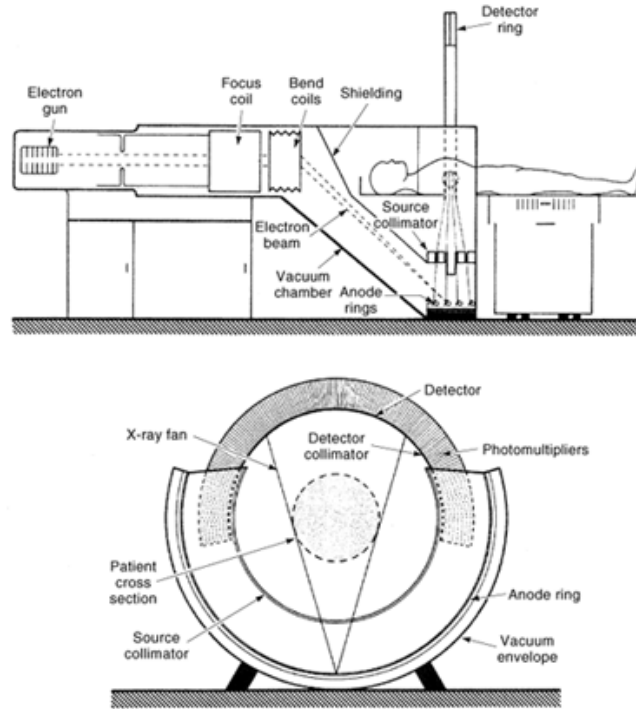
Fig. 3. Electronic steering of an X-ray beam for motion-free scanning and *CT* imaging. (Reproduced with permission from D. P. Boyd et al., Proposed dynamic cardiac 3-D densitometer for early detection and evaluation of heart disease, *IEEE Trans. Nucl. Sci.*, **NS-26**: pp. 2724–2727, 1979. Copyright © 1979 IEEE. See also Ref. 22.)

- *Photon Detection Noise.* The interaction between an X-ray beam and a detector is governed by the same rules as for interaction with any other matter: photons are lost due to scatter and absorption, and some photons may pass through unaffected (undetected). The small size of the detectors in *CT* imaging reduces their detection efficiency. Scattered and undetected photons cause noise in the measurement; for detailed analysis of noise in X-ray detection, please refer to 29 and Cho et al. (28).
- *Ray Stopping by Heavy Implants.* If the body imaged contains extremely heavy parts or components that are nearly X-ray opaque and stop entirely the incoming X-ray photons (such as metal screws or plates in bones and surgical clips), no photons would be detected at the corresponding point of exit from the body. Effectively, the attenuation coefficient for the corresponding path would be infinite. A reconstruction algorithm would not be able to redistribute such an attenuation value over the pixels along the corresponding ray path in the reconstructed image. This leads to streaking artifacts in *CT* images.

Other imaging modalities used for projection data collection are ultrasound (time of flight or attenuation), magnetic resonance (*MR*), and nuclear emission (gamma rays or positrons) (12, 17, 28, 29, 3233–34). Techniques using nonionizing radiation are of importance in imaging pregnant women and/or fetuses. While the physical parameter imaged may differ between these modalities, once the projection data are acquired, the mathematical image reconstruction procedure could be almost the same. A few special considerations in imaging with diffracting sources are described in the section entitled "Imaging with Diffracting Sources." The nature of data acquired in *MR* imaging is described in the section entitled "Nature of Data Acquired in Magnetic Resonance Imaging."

Image Reconstruction Techniques

Projection Geometry.   Let us now consider the problem of reconstructing a 2-D image given parallel-ray projections of the image measured at different angles. Referring to Fig. 4, let f(x, y) represent the density distribution within the image. While in practice discrete images are used, the initial presentation here will be in continuous space notations for easier comprehension. Consider a ray AB represented by the equation

$$x \cos \theta + y \sin \theta = t_1$$

[The derivations presented in this article follow closely those of 13; we thank them for their kind permission. For further details, please refer to 17, 18) and Kak and Slaney (12).] The integral of f(x, y) along the ray path AB is given by

$$P_\theta(t_1) = \int_{AB} f(x, y) \, ds$$
$$= \int_{-\infty}^{\infty} \int_{-\infty}^{\infty} f(x, y)\delta(x \cos \theta + y \sin \theta - t_1) \, dx \, dy$$

where $\delta(\cdot)$ is the Dirac delta function. When this integral is evaluated for different values of the ray offset t_1, we obtain the projection $P_\theta(t)$. The function $P_\theta(t)$ is known as the *Radon transform* of f(x, y). [Note that while a single projection $P_\theta(t)$ of a 2-D image at a given value of θ is a 1-D function, a set of projections for various values of θ could be seen as a 2-D function.] As the different rays within a projection are parallel to one another, this is known as parallel-ray geometry.

Theoretically, we would need an infinite number of projections for all θ to be able to reconstruct the image. Before we consider reconstruction techniques, let us take a look at the projection or Fourier slice theorem.

The Projection or Fourier Slice Theorem.   The projection or Fourier slice theorem relates the three spaces we encounter in image reconstruction from projections—the image, Fourier, and projection (Radon) spaces. Considering a 2-D image, the theorem states that the 1-D Fourier transform (*FT*) of a 1-D projection of the 2-D image is equal to the radial section (slice) of the 2-D *FT* of the 2-D image at the angle of the projection. This is illustrated graphically in Fig. 5 and may be derived as follows.

Let $F(u, v)$ represent the 2-D *FT* of f(x, y), given by

$$F(u, v) = \int_{-\infty}^{\infty} \int_{-\infty}^{\infty} f(x, y) \exp[-j2\pi(ux + vy)] \, dx \, dy$$

Let $S_\theta(w)$ represent the 1-D *FT* of the projection $P_\theta(t)$; that is,

$$S_\theta(w) = \int_{-\infty}^{\infty} P_\theta(t) \exp(-j2\pi wt) \, dt$$

where w represents the frequency variable corresponding to t . (*Note*: if $x, y, s,$ and t are in centimeters, the units for $u, v,$ and w will be cycles/cm.) Let $f(t, s)$ represent the image f(x, y) rotated by angle θ, with the transformation given by

$$\begin{bmatrix} t \\ s \end{bmatrix} = \begin{bmatrix} \cos \theta & \sin \theta \\ -\sin \theta & \cos \theta \end{bmatrix} \begin{bmatrix} x \\ y \end{bmatrix}$$
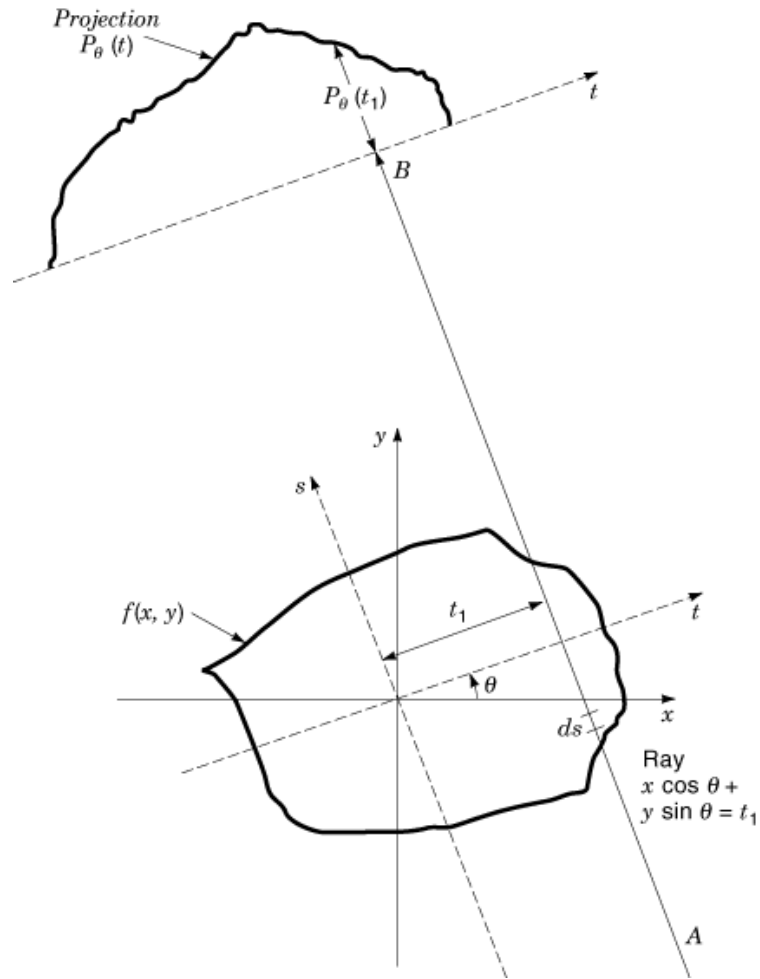
Fig. 4.   Illustration of a ray path *AB* through a sectional image $f(x, y)$. The (t, s) axis system is rotated by angle θ with respect to the (x, y) axis system. *ds* represents the elemental distance along the ray path AB. $P_\theta (t_1)$ is the ray integral of $f(x, y)$ for the ray path *AB*. $P_\theta (t)$ is the parallel-ray projection (Radon transform or integral) of $f(x, y)$ at angle θ. (Adapted with permission from A. Rosenfeld and A. C. Kak, *Digital Picture Processing*, 2nd ed., New York: Academic Press. Copyright © 1982 Academic Press.)

Then

$$P_\theta(t) = \int_{-\infty}^{\infty} f(t, s)\, ds$$

$$S_\theta(w) = \int_{-\infty}^{\infty} P_\theta(t)\exp(-j2\pi wt)\, dt$$

$$= \int_{-\infty}^{\infty} \left[\int_{-\infty}^{\infty} f(t, s)ds \right] \exp(-j2\pi wt)\, dt$$
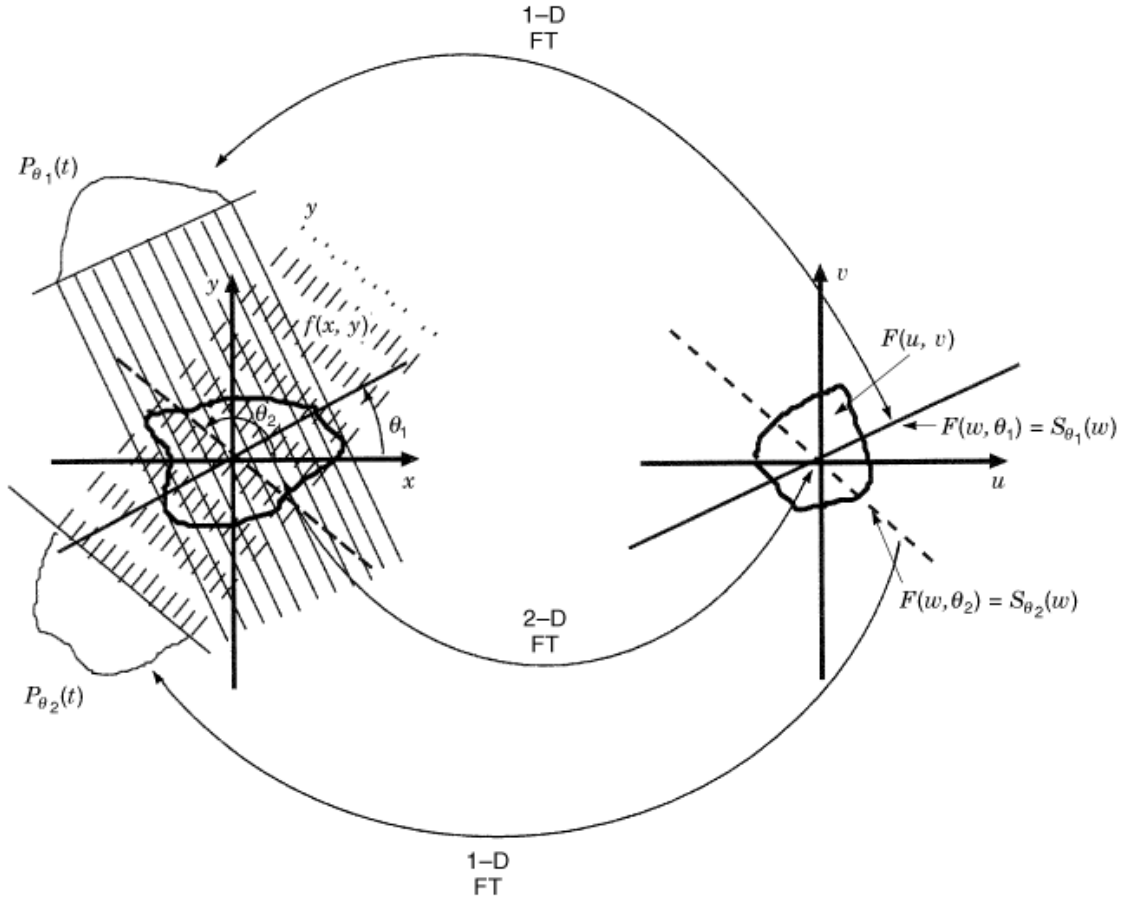
Fig. 5. Illustration of the Fourier slice theorem. $F(u, v)$ is the 2-D *FT* of $f(x, y)$. $F(w, \theta_1) = S_{\theta_1}(w)$ is the 1-D *FT* of $P_{\theta_1}(t)$. $F(w, \theta_2) = S_{\theta_2}(w)$ is the 1-D *FT* of $P_{\theta_2}(t)$.

Transforming from (t, s) to (x, y), we get

$$S_\theta(w) = \int_{-\infty}^{\infty} \int_{-\infty}^{\infty} f(x, y) \exp[-j2\pi w(x \cos \theta$$
$$+ y \sin \theta)] dx dy$$
$$= F(u, v) \quad \text{for } u = w \cos \theta, \ v = w \sin \theta$$
$$= F(w, \theta)$$

which expresses the projection theorem. Note that $dxdy = dsdt$.

It immediately follows that if we have projections available at all angles from $0°$ to $180°$, we can take their 1-D FTs, fill the 2-D Fourier space with the corresponding radial sections or slices, and take an inverse 2-D *FT* to obtain the image $f(x, y)$. The difficulty lies in the fact that, in practice, only a finite number of projections will be available, measured at discrete angular positions or steps. Thus some form of interpolation will be essential in the 2-D Fourier space (5, 6). Extrapolation may also be required if the given projections do not span the

entire angular range. This method of reconstruction from projections, known as the Fourier method, succinctly relates the image, Fourier, and projection (Radon) spaces.

Backprojection.   Let us now consider the simplest reconstruction procedure—backprojection (*BP*). Assuming the rays to be ideal straight lines (rather than strips of finite width) and the image to be made of dimensionless points rather than pixels or voxels of finite size, it can be seen that each point in the image $f(\mathrm{x}, \mathrm{y})$ contributes to only one ray integral per parallel-ray projection $P_\theta(t)$, with $t = x \cos \theta + y \sin \theta$. We may obtain an estimate of the density at a point by simply summing (integrating) all the rays that pass through it at various angles, that is, by backprojecting the individual rays. In doing so, however, the contributions to the various rays of all other points along their paths are also added up, causing smearing or blurring; yet this method produces a reasonable estimate of the image. Mathematically, simple *BP* can be expressed as (13)

$$f(x, y) \simeq \int_0^\pi P_\theta(t)\, d\theta, \quad \text{where } t = x \cos \theta + y \sin \theta$$

This is a sinusoidal path of integration in the (θ, t) Radon space. In practice, only a finite number of projections and a finite number of rays per projection will be available—that is, the (θ, t) space will be discretized—hence interpolation will be required.

Considering a point source as the image to be reconstructed, it can be seen that *BP* produces a spoke-like pattern with lines at all projection angles, intersecting at the position of the point source. This may be considered to be the point spread function (*PSF*) of the reconstruction process, which is responsible for the blurring of details (please see the section entitled "Examples of Reconstructed Images" for illustrations of the *PSF* of the *BP* process). Because the *BP* procedure is linear, the reconstructed version of an unknown image may be modeled as the convolution of the unknown image with the PSF. Knowing the PSF, we may attempt deconvolution. Deconvolution is implicit in the filtered (convolution) backprojection technique, which is described next.

Filtered Backprojection.   Consider the inverse *FT* relationship

$$f(x, y) = \int_{-\infty}^{\infty} \int_{-\infty}^{\infty} F(u, v) \exp[j2\pi(ux + vy)]\, du\, dv$$

Changing from (u, v) to polar coordinates (w, θ), we get

$$\begin{aligned}
f(x, y) &= \int_0^{2\pi} \int_0^\infty F(w, \theta) \exp[j2\pi w(x \cos \theta \\
&\quad + y \sin \theta)]\, w\, dw\, d\theta \\
&= \int_0^\pi \int_0^\infty F(w, \theta) \exp[j2\pi w(x \cos \theta \\
&\quad + y \sin \theta)]\, w\, dw\, d\theta \\
&\quad + \int_0^\pi \int_0^\infty F(w, \theta + \pi) \exp\{j2\pi w[x \cos(\theta + \pi) \\
&\quad + y \sin(\theta + \pi)]\}\, w\, dw\, d\theta
\end{aligned}$$

Here, $u = w\cos\theta$, $v = w\sin\theta$, and $dudv = wdwd\theta$. Since $F(w, \theta + \pi) = F(-w, \theta)$, we get

$$f(x, y) = \int_0^{\pi} \left[\int_{-\infty}^{\infty} F(w, \theta)|w| \exp(j2\pi wt)\, dw \right] d\theta$$

$$= \int_0^{\pi} \left[\int_{-\infty}^{\infty} S_\theta(w)|w| \exp(j2\pi wt)\, dw \right] d\theta \qquad (2)$$

where again $t = x \cos\theta + y \sin\theta$. If we now define

$$Q_\theta(t) = \int_{-\infty}^{\infty} S_\theta(w)|w| \exp(j2\pi wt)\, dw$$

we get

$$f(x, y) = \int_0^{\pi} Q_\theta(t)\, d\theta = \int_0^{\pi} Q_\theta(x \cos\theta + y \sin\theta)\, d\theta$$

It is now seen that a perfect reconstruction of f(x, y) may be obtained by backprojecting *filtered* projections $Q_\theta(t)$ instead of backprojecting the original projections $P_\theta(t)$) hence the name *filtered backprojection* (*FBP*). The filter is represented by the $|w|$ function, known as the *ramp filter*.

Note that the limits of integration in Eq. (2) are $(0, \pi)$ for θ and $(-\infty, \infty)$ for w. In practice, a smoothing window should be applied to reduce the effects of high-frequency noise. Furthermore, the integrals change to summations in practice due to the finite number of projections available, as well as the discrete nature of the projections themselves and the *FT* computations employed. (Details of the discrete version of *FBP* are provided in the section entitled "Discrete Filtered Backprojection.")

An important feature of the *FBP* technique is that each projection may be filtered and backprojected as other projections are being acquired, which was of help in online processing with the first-generation scanners. Furthermore, the inverse *FT* of the filter $|w|$ (with modifications to account for the discrete nature of measurements, smoothing window, etc.) could be used to convolve the projections directly in the t space (7) using fast array processors. *FBP* is the most widely used procedure for image reconstruction from projections; however, the procedure provides good reconstructed images only when a large number of projections spanning the full angular range of 0° to 180° are available.

Discrete Filtered Backprojection.   The filtering procedure with the $|w|$ function, in theory, must be performed over $-\infty \le w \le \infty$. In practice, the signal energy above a certain frequency limit will be negligible, and $|w|$ filtering beyond the limit increases noise. Thus we may consider the projections to be bandlimited to $\pm W$ cycles/cm. Then, using the sampling theorem, $P_\theta(t)$ can be represented by its samples at the sampling rate $2W$ cycles/cm as

$$P_\theta(t) = \sum_{k=-\infty}^{\infty} P_\theta\left(\frac{k}{2W}\right) \frac{\sin 2\pi W(t - k/2W)}{2\pi W(t - k/2W)}$$

Then

$$S_\theta(w) = \frac{1}{2W} \sum_{k=-\infty}^{\infty} P_\theta\left(\frac{k}{2W}\right) \exp\left[-j2\pi w\left(\frac{k}{2W}\right)\right] b_W(w)$$

$$b_W(w) = 1, \quad |w| \le W$$
$$= 0, \quad \text{otherwise} \tag{3}$$

If the projections are of finite order, that is, they can be represented by a finite number of samples $N + 1$, then

$$S_\theta(w) = \frac{1}{2W} \sum_{k=-N/2}^{N/2} P_\theta\left(\frac{k}{2W}\right) \exp\left[-j2\pi w\left(\frac{k}{2W}\right)\right] b_W(w)$$

Assume that N is even, and let the frequency axis be discretized as

$$S_\theta\left(m\frac{2W}{N}\right) = \frac{1}{2W} \sum_{k=-N/2}^{N/2} P_\theta\left(\frac{k}{2W}\right) \exp\left(-j2\pi m\frac{k}{N}\right)$$

Then

$$m = -\frac{N}{2}, \ldots, 0, \ldots, \frac{N}{2}$$

This represents the discrete *FT* (*DFT*) relationship and may be evaluated using the fast Fourier transform (*FFT*) algorithm.

The filtered projection $Q_\theta(n \ \tau)$ may be obtained as

$$Q_\theta(t) = \int_{-W}^{W} S_\theta(w)|w| \exp(j2\pi wt)\, dw$$

$$\simeq \frac{2W}{N} \sum_{m=-N/2}^{N/2} S_\theta\left(m\frac{2W}{N}\right)\left|m\frac{2W}{N}\right| \exp\left[j2\pi m\left(\frac{2W}{N}\right)t\right]$$

If we want to evaluate $Q_\theta(t)$ for only those t at which $P_\theta(t)$ has been sampled, we get

$$Q_\theta\left(\frac{k}{2W}\right) \simeq \frac{2W}{N} \sum_{m=-N/2}^{N/2} S_\theta\left(m\frac{2W}{N}\right)\left|m\frac{2W}{N}\right| \exp\left(j2\pi m\frac{k}{N}\right)$$

$$k = -\frac{N}{2}, \ldots, -1, 0, 1, \ldots, \frac{N}{2}$$

In order to control noise enhancement by the $|(m(2W/N)|$ filter, it may be beneficial to include a filter window such as the Hamming window; then

$$Q_\theta \left(\frac{k}{2W} \right)$$

$$\simeq \frac{2W}{N} \sum_{m=-N/2}^{N/2} S_\theta \left(m \frac{2W}{N} \right) \left| m \frac{2W}{N} \right| G \left(m \frac{2W}{N} \right) \exp \left(j2\pi m \frac{k}{N} \right)$$

with

$$G \left(m \frac{2W}{N} \right)$$

$$= 0.54 + 0.46 \cos \left(m \frac{2W}{N} \frac{\pi}{W} \right), \quad m = -\frac{N}{2}, \ldots, 0, \ldots, \frac{N}{2}$$

Using the convolution theorem, we get

$$Q_\theta \left(\frac{k}{2W} \right) \simeq \frac{2W}{N} P_\theta \left(\frac{k}{2W} \right) * \phi \left(\frac{k}{2W} \right)$$

where denotes circular (periodic) convolution, and $\phi(k/2W)$ is the inverse *DFT* of $|m(2W/N)|\ G(m(2W/N))$, $m = -N/2, \ldots, 0, \ldots, N/2$. Butterworth or other lowpass filters may also be used instead of the Hamming window.

Note that the inverse *FT* of $|w|$ does not exist as $|w|$ is not square integrable. However, if we consider the inverse *FT* of $|w| \exp(-\epsilon verbar;w|)$ as $\epsilon \to 0$, we get the function (13)

$$p_\epsilon(t) = \frac{\epsilon^2 - (2\pi t)^2}{[\epsilon^2 + (2\pi t)^2]^2}$$

For large t, $p_\varepsilon(t) \simeq -1/(2\pi t)^2$.

The reconstructed image may be obtained as

$$\hat{f}(x, y) = \frac{\pi}{K} \sum_{i=1}^{K} Q_{\theta_i} (x \cos \theta_i + y \sin \theta_i)$$

where the K angles θ_i are those at which projections $P_\theta(t)$ are available.

For practical implementation of discrete *FBP*, let the projections be sampled with an interval of τ cm with no aliasing error. Each projection $P_\theta(k_\tau)$ is thus limited to the frequency band $(-W, W)$, with $W = (1/2\tau)$ cycles/cm. The continuous versions of the filtered projections are

$$Q_{\theta_i}(t) = \int_{-\infty}^{\infty} S_{\theta_i}(w) H(w) \exp(j2\pi wt) \, dw$$

where the filter $H(w) = |w|b_{\mathrm{W}}(w)$, with $b_{\mathrm{W}}(w)$ as defined earlier in Eq. (3). The impulse response of the filter $H(w)$ is (13)

$$h(t) = \frac{1}{2\tau^2}\frac{\sin(2\pi t/2\tau)}{2\pi t/2\tau} - \frac{1}{4\tau^2}\left(\frac{\sin(\pi t/2\tau)}{\pi t/2\tau}\right)^2$$

Since we require $h(t)$ only at integral multiples of the sampling interval τ, we have

$$h(n\tau) = \begin{cases} \dfrac{1}{4\tau^2}, & n = 0 \\ 0, & n \text{ even} \\ -\dfrac{1}{n^2\pi^2\tau^2}, & n \text{ odd} \end{cases}$$

The filtered projection $Q_\theta(t)$ may be obtained as

$$Q_{\theta_i}(n\tau) = \tau\sum_{k=0}^{N-1} P_{\theta_i}(k\tau)h(n\tau - k\tau), \quad n = 0, 1, \ldots, N-1$$

where N is the finite number of samples in the projection $P_{\theta i}(k_\tau)$. Note that $h(n_\tau)$ is required for $n = -(N-1)$, . . ., 0, . . ., $N-1$. When the filter is implemented as a convolution, the *FBP* method is also referred to as *convolution backprojection*.

The procedure for *FBP* may be expressed in algorithmic form as:

(1) Measure projection $P_{\theta_i}(n\ \tau)$.
(2) Compute the filtered projection $Q_{\theta_i}(n\tau)$.
(3) Backproject the filtered projection $Q_{\theta_i}(n\tau)$.
(4) Repeat Steps 1 to 3 for all projection angles $\theta_i, i = 1, 2, \ldots, K$.

Severe artifacts arise if sampling in the (θ, t) space is inadequate or incomplete. The *FBP* algorithm is suitable for online implementation in a *translate–rotate CT* scanner as each parallel-ray projection may be filtered and backprojected as soon as it is acquired, while the scanner is acquiring the next projection. The reconstructed image is ready as soon as the last projection is acquired, filtered, and backprojected. When the projections are acquired using fan-beam geometry, one could either re-bin the fan-beam data to compose parallel-ray projections, or use reconstruction algorithms specifically tailored to fan-beam geometry (12, 13).

Algebraic Reconstruction Techniques.   In the absence of complete projection data spanning the full angular range of $0°$ to $180°$, the algebraic reconstruction technique (*ART*) (19, 20) could yield better results than *FBP* or the Fourier method. *ART* is related to the Kaczmarz method of projections for solving simultaneous equations [see Rosenfeld and Kak (13) for an excellent discussion on this topic].

The Kaczmarz method takes an approach that is completely different from that of the Fourier or *FBP* methods: the available projections (ray sums in the discrete case) are seen as a set of simultaneous equations, with the unknown quantities being discrete pixels of the image. The large sizes of images encountered in practice preclude the use of the usual methods for solving simultaneous equations. Furthermore, in many practical applications, the number of available equations may be far less than the number of pixels in the image to be reconstructed; the set of simultaneous equations is then underdetermined. The Kaczmarz method of projections is an elegant iterative method, which may be implemented easily.
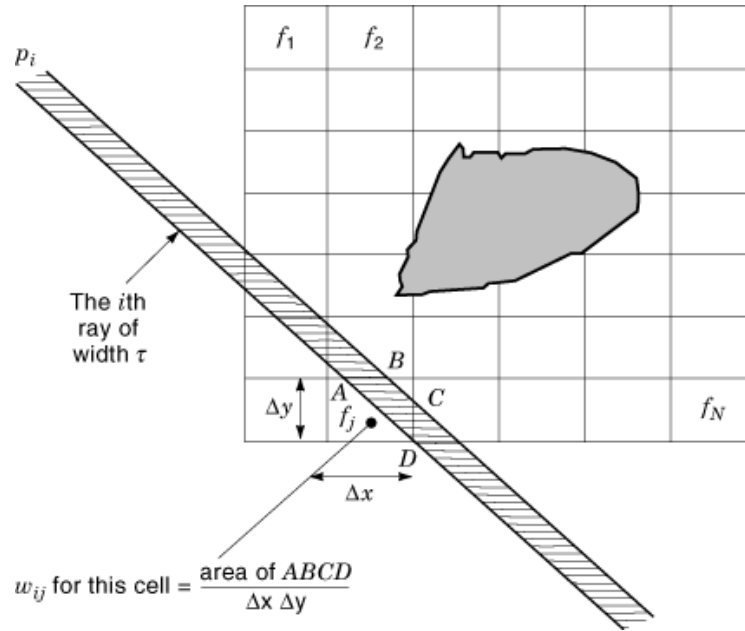
Fig. 6. *ART* treats the image as a matrix of discrete pixels of finite size (Δx, Δy). Each ray has a finite width. The fraction of the area of the *j*th pixel crossed by the *i*th ray is represented by the weighting factor w_{ij} . w_{ij} = Area of *ABCD*/(Δx Δy) for the *j*th pixel in the figure. (Adapted with permission from A. Rosenfeld and A. C. Kak, *Digital Picture Processing*, 2nd ed., New York: Academic Press. Copyright © 1982 Academic Press.)

Let the image to be reconstructed be divided into N cells, f_i denoting the value in the *j*th cell (the image density or intensity is assumed to be constant within each cell). Let M ray sums be made available, expressed as

$$p_i = \sum_{j=1}^{N} w_{ij} f_j, \;\; i = 1, 2, \ldots, M$$

where w_{ij} is the contribution factor of the *j*th image element to the *i*th ray sum, equal to the fractional area of the *j*th cell crossed by the *i*th ray path, as illustrated in Fig. 6. Note that for a given ray i, most of the w_{ij} will be zero, as only a few elements of the image contribute to the corresponding ray sum. Then

$$\begin{aligned}
w_{11} f_1 + w_{12} f_2 + \cdots + w_{1N} f_N &= p_1 \\
w_{21} f_1 + w_{22} f_2 + \cdots + w_{2N} f_N &= p_2 \\
&\;\;\vdots \\
w_{M1} f_1 + w_{M2} f_2 + \cdots + w_{MN} f_N &= p_M
\end{aligned}$$

A grid representation with N cells gives the image N degrees of freedom. Thus an image represented by $(f_1, f_2, \ldots, f_N)$ may be considered to be a single point in an N-dimensional hyperspace. Thus each of the above ray sum equations will represent a hyperplane in this hyperspace. If a unique solution exists, it is given by the intersection of all the hyperplanes at a single point. To arrive at the solution, the Kaczmarz method takes the

approach of successively and iteratively projecting an initial guess and its successors from one hyperplane to the next.

Let us, for simplicity, consider a 2-D version of the situation, as illustrated in Fig. 7. Let $f^{(0)}$ represent vectorially the initial guess to the solution, and let $\mathbf{w}_1$ represent vectorially the series of weights (coefficients) in the first ray equation. The first ray sum may then be written as

$$\boldsymbol{w}_1 \cdot \boldsymbol{f} = p_1 \tag{4}$$

The hyperplane represented by this equation is orthogonal to $\boldsymbol{w}_1$. With reference to Fig. 8, Eq. (4) says that for the vector OC corresponding to any point C on the hyperplane, its projection onto the vector $\mathbf{w}_1$ is of a constant length. The unit vector OU along $\boldsymbol{w}_1$ is given by

$$OU = \frac{w_1}{\sqrt{w_1 \cdot w_1}}$$

The perpendicular distance of the hyperplane from the origin is

$$|OA| = OU \cdot OC = \frac{w_1 \cdot f}{\sqrt{w_1 \cdot w_1}} = \frac{p_1}{\sqrt{w_1 \cdot w_1}}$$

Now, $\boldsymbol{f}^{(1)} = \boldsymbol{f}^{(0)} - \boldsymbol{GH}$, and

$$
\begin{aligned}
|GH| = |OF| - |OA| &= f^{(0)} \cdot OU - |OA| \\
&= \frac{f^{(0)} \cdot w_1}{\sqrt{w_1 \cdot w_1}} - \frac{p_1}{\sqrt{w_1 \cdot w_1}} \\
&= \frac{(f^{(0)} \cdot w_1 - p_1)}{\sqrt{w_1 \cdot w_1}}
\end{aligned}
$$

Since the directions of GH and OU are the same, $GH = |GH|\, OU$. Thus

$$GH = \left(\frac{f^{(0)} \cdot w_1 - p_1}{\sqrt{w_1 \cdot w_1}} \right) \frac{w_1}{\sqrt{w_1 \cdot w_1}} = \left(\frac{f^{(0)} \cdot w_1 - p_1}{w_1 \cdot w_1} \right) w_1$$

Therefore

$$f^{(1)} = f^{(0)} - \left(\frac{f^{(0)} \cdot w_1 - p_1}{w_1 \cdot w_1} \right) w_1$$

In general, the jth estimate is obtained from the $(j-1)$th estimate as

$$f^{(j)} = f^{(j-1)} - \left(\frac{f^{(j-1)} \cdot w_j - p_j}{w_j \cdot w_j} \right) w_j \tag{5}$$
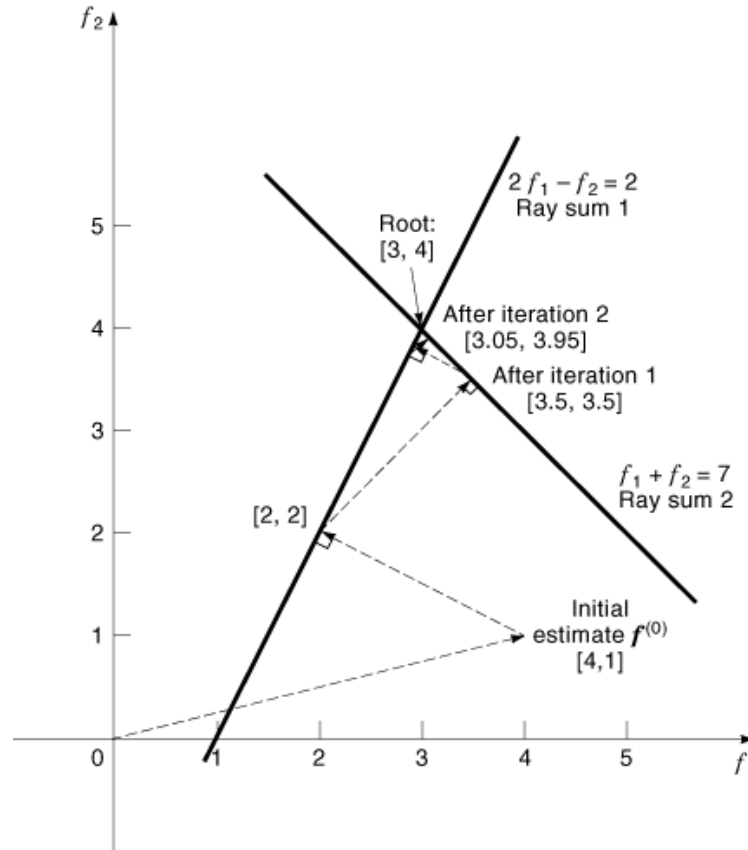
Fig. 7.   Illustration of the Kaczmarz method of solving a pair of simultaneous equations in two unknowns. The solution is $f = [3, 4]'$. The weight vectors for the two ray sums (straight lines) are $w_1 = [2, -1]'$ and $w_2 = [1, 1]'$. The equations of the straight lines are $w_1 \cdot f = 2f_1 - f_2 = 2 = p_1$ and $w_2 \cdot f = f_1 + f_2 = 7 = p_2$. The initial estimate is $f^{(0)} = [4, 1]'$. The first updated estimate is $f^{(1)} = [2, 2]'$; the second updated estimate is $f^{(2)} = [3.5, 3.5]'$. As two ray sums are given, two corrections constitute one cycle (or iteration) of ART. The path of the second cycle of ART is also illustrated in the figure.

That is, the current (jth − 1)th estimate is projected onto the jth projection hyperplane and the deviation from the true ray sum p_j is obtained. This deviation is normalized and applied as a correction to all the pixels according to the weighting factors w. When this process is applied to all the M ray sum hyperplanes given, one cycle or iteration is completed.

Depending on the initial guess and the arrangement of the hyperplanes, a number of iterations may have to be completed in order to obtain the solution (if it exists). The following characteristics of ART are worth noting:

- ART proceeds ray-by-ray and is iterative.
- If the hyperplanes of all the given projections are mutually orthogonal, we may start with any initial guess and reach the solution in only one cycle (if it exists). On the other hand, if the hyperplanes subtend very small angles with one another, a large number of iterations will be required. The number of iterations required may be reduced by using optimized projection access schemes (35).
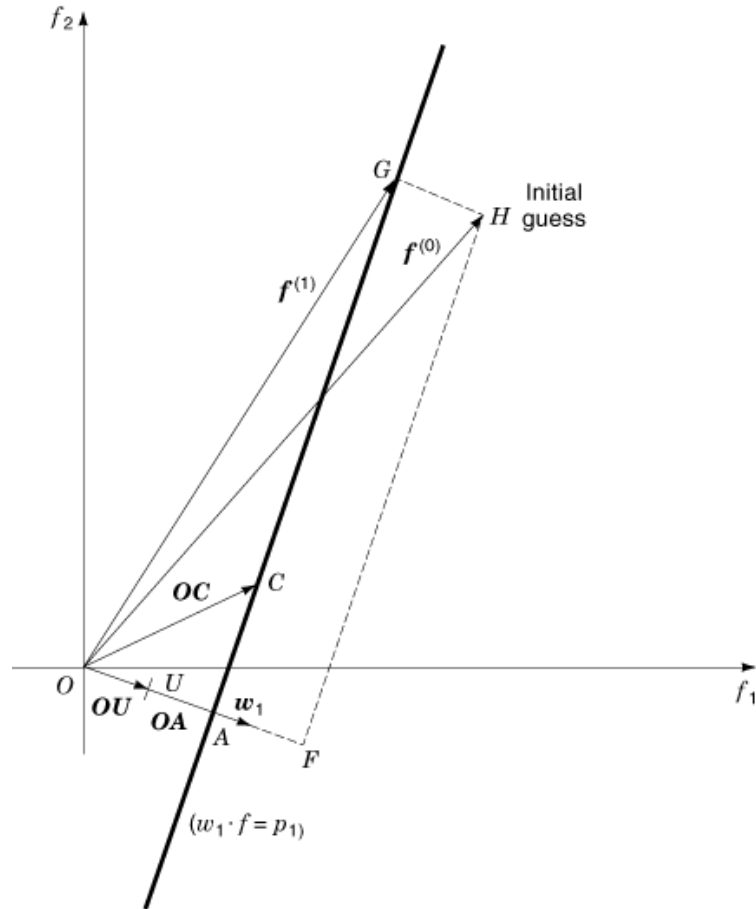
Fig. 8.   Illustration of the algebraic reconstruction technique. $\boldsymbol{f}^{(1)}$ is an improved estimate computed by projecting the initial estimate $\boldsymbol{f}^{(0)}$ onto the hyperplane (the straight line AG in the illustration) corresponding to the first ray sum given by the equation $\boldsymbol{w}_1 \cdot \boldsymbol{f} - p_1$. (Reproduced with permission from A. Rosenfeld and A. C. Kak, *Digital Picture Processing*, 2nd ed., New York: Academic Press. Copyright © 1982 Academic Press.)

- If the number of ray sums is greater than the number of pixels, that is, $M \geq N$, but the measurements are noisy, no unique solution exists—the procedure will oscillate in the neighborhood of the intersections of the hyperplanes.
- If $M < N$, the system is underdetermined and an infinite number of solutions will exist. It has been shown that unconstrained ART converges to the minimum-variance estimate (36).
- The major advantage of ART is that any *a priori* information about the image may be introduced easily into the iterative procedure (e.g., upper or lower limits on pixel values, spatial boundaries of the image). This may help in obtaining a useful "solution" even if the system is underdetermined.

Approximations to the Kaczmarz Method.   We could rewrite the reconstruction step in Eq. (5) at the pixel level as

$$f_m^{(j)} = f_m^{(j-1)} + \left(\frac{(p_j - q_j)}{\sum_{k=1}^{N} w_{jk}^2} \right) w_{jm} \qquad (6)$$

where $q_j = \boldsymbol{f}^{(i-1)} \cdot \boldsymbol{w}_j = \Sigma_{k=1}^{N} f^{(j-1)}_k \, \boldsymbol{w}_{jk}$. This equation says that when we project the $(j-1)$th estimate onto the jth hyperplane, the correction factor for the mth cell is

$$\Delta f_m^{(j)} = f_m^{(j)} - f_m^{(j-1)} = \left(\frac{(p_j - q_j)}{\sum_{k=1}^{N} w_{jk}^2} \right) w_{jm}$$

Here, p_j is the given (true) ray sum for the jth ray, and q_j is the computed ray sum for the same ray for the estimated image on hand. $(p_j - q_j)$ is the error in the estimate, which may be normalized and applied as a correction to all the pixels with appropriate weighting. In one of the approximations (19, 20), the w_{jk} are simply replaced by 0's or 1's depending on whether the center of the jth image cell is within the ith ray (of finite width) or not. Then the coefficients need not be computed and stored: we may instead determine the pixels to be corrected for the ray considered during the reconstruction procedure. Furthermore, $\Sigma_{k=1}^{N} w^{2jk}_{jk>} = N_j$, the number of pixels crossed by the jth ray. The correction to *all pixels* in the jth ray is then $(p_j - q_j)/N_j$. Thus

$$f_m^{(j)} = f_m^{(j-1)} + \frac{(p_j - q_j)}{N_j} \qquad (7)$$

Because the corrections may be negative, negative pixel values may be encountered. Since negative values are not meaningful in most imaging applications, the constrained (and thereby nonlinear) version of *ART* is defined as

$$f_m^{(j)} = \max \left[0, \ f_m^{(j-1)} + \frac{(p_j - q_j)}{N_j} \right] \qquad (8)$$

The corrections could also be multiplicative (8):

$$f_m^{(j)} = f_m^{(j-1)} + \frac{p_j}{q_j} \qquad (9)$$

In this case no positivity constraint is required. Furthermore, the convex hull of the image is almost guaranteed (subject to approximation related to the number of projections available), as a pixel once set to zero will remain so during subsequent iterations. It has been shown that the multiplicative version of *ART* converges to the maximum-entropy estimate of the image (18, 37).

A generic *ART* procedure may be expressed in the following algorithmic form:

(1) Prepare an initial estimate of the image. All of the pixels in the initial image could be zero for additive ART; however, for multiplicative ART, pixels within at least the convex hull of the object in the image must be nonzero.
(2) Compute the projection (or ray sum) q_j for the first ray path for the initial estimate of the image.

(3) Obtain the difference between the true ray sum p_j and the computed ray sum q_j, and apply the correction to all the pixels belonging to the ray according to one of the *ART* equations [e.g., Eq. (6), (7), (8) or (9)]. Apply constraints, if any, based on *a priori* information available.

(4) Perform Steps 2 and 3 for all rays available.

(5) Steps 2 to 4 constitute one cycle or iteration (over all available projections or ray sums). Repeat Steps 2 to 4 as many times as required. If desired, compute a measure of convergence, such as

$$E = \sum_{j=1}^{M} (p_j - q_j)^2$$

Stop if the error is less than a prespecified limit; else, go back to Step 2.

For improved convergence, a simultaneous correction procedure [simultaneous iterative reconstruction technique—SIRT (38)] has been proposed, where the corrections to all pixels from all the rays are first computed, and the averaged corrections are applied at the same time to all the pixels (i.e., only one correction is applied per pixel per iteration). Guan and Gordon (35) proposed different projection access schemes to improve convergence, including consecutive use of projections in mutually orthogonal directions.

Imaging with Diffracting Sources.   In some applications of *CT* imaging, such as imaging pregnant women, X-ray imaging might not be advisable. Imaging with nonionizing forms of radiation, such as acoustic (ultrasonic) (12, 32) and electromagnetic (optical or thermal) imaging (34), is then a valuable alternative. X-ray imaging is also not suitable when the object to be imaged has no (or poor) contrast in density or atomic number distribution. An important point to note in acoustic or electromagnetic imaging is that these forms of energy do not propagate along straight-line ray paths through a body due to refraction and diffraction. When the dimensions of inhomogeneities in the object being imaged are comparable to or smaller than the wavelength of the radiation used, geometric propagation concepts cannot be applied; it becomes necessary to consider wave propagation and diffraction-based methods.

When the body being imaged may be treated as a weakly scattering object in the 2-D sectional plane and invariant in the axial direction, the Fourier diffraction theorem is applicable (12). This theorem states that the *FT* of a projection including the effects of diffraction gives values of the 2-D *FT* of the image along a semicircular arc. Interpolation methods may be developed in the Fourier space taking this property into account for reconstruction of images from projections obtained with diffracting sources. Backpropagation and algebraic techniques have also been proposed for the case of imaging with diffracting sources (12). Detailed discussion of these methods is beyond the scope of the present article.

Nature of Data Acquired in Magnetic Resonance Imaging.   MR imaging is based on the principle of nuclear magnetic resonance (*NMR*)—the behavior of nuclei under the influence of externally applied magnetic and electromagnetic (radio-frequency or RF) fields (28, 33, 39). A nucleus with an odd number of protons or an odd number of neutrons has an inherent nuclear spin and exhibits a magnetic moment; such a nucleus is said to be *NMR* active. The commonly used modes of *MR* imaging rely on hydrogen[1]H (proton), carbon[13]C, fluorine[19]F, and phosphorus[31]P nuclei.

In the absence of an external magnetic field, the vectors of magnetic moments of active nuclei have random orientations, resulting is no net magnetism. When a strong external magnetic field H_0 is applied, the nuclear spins of active nuclei align with the field (either parallel or antiparallel to the field). The axis of the magnetic field is referred to as the z axis. Parallel alignment corresponds to a lower energy state than antiparallel alignment, and hence there will be more nuclei in the former state. This state of forced alignment results in a net magnetization vector.

The magnetic spin vector of each active nucleus precesses about the z axis at a frequency known as the Larmor frequency, given by $\omega_0 = -\gamma H_0$, where γ is the gyromagnetic ratio of the nucleus considered. This form of precession is comparable to the rotation of a spinning top's axis around the vertical.

MR imaging involves controlled perturbation of the precession of nuclear spins and measurement of the RF signals emitted when the perturbation is stopped and the nuclei return to their previous states. *MR* imaging is an intrinsically 3-D imaging procedure. The traditional *CT* scanners require mechanical scanning and provide 2-D cross-sectional or transversal images in a slice-by-slice manner. Slices at other orientations, if required, have to be computed from a set of 2-D slices covering the required volume. In *MR* imaging, however, images may be obtained directly at any transversal, coronal, sagittal, or oblique section by using appropriate gradients and pulse sequences. Furthermore, no mechanical scanning is involved: slice selection and scanning are performed electronically by the use of magnetic field gradients and RF pulses.

The main components and principles of *MR* imaging are (33):

- A *magnet* that provides a strong, uniform field of the order of 0.5 to 4 T. This causes all active nuclei to align in the direction of the field (parallel or antiparallel) and precess about the axis of the field. The rate of precession is proportional to the strength of the magnetic field H_0 . The stronger the magnetic field, the higher will be the signal-to-noise ratio of the data acquired.
- An *RF transmitter* to deliver an RF electromagnetic pulse H_1 to the body being imaged. The RF pulse provides the perturbation: it causes the axis of precession of the spin vectors to deviate or "flip" from the z axis. In order for this to happen, the frequency of the RF field must be the same as that of precession of the active nuclei, such that the nuclei can absorb energy from the RF field (hence the term "resonance"). The frequency of RF-induced rotation is given by $\omega_1 = -\gamma H_1$. When the RF perturbation is removed, the active nuclei return to their unperturbed states (alignment with H_0) through various relaxation processes, emitting energy as RF signals.
- A *gradient system* to apply to the body a controlled, spatially varying and time-varying magnetic field $h(x) = G \cdot x$, where x is a vector representing the spatial coordinates and G is the gradient applied. The components of G along the z direction as well as in the x and y directions (the plane orthogonal to the z axis) are controlled individually. The gradient causes nuclei at different positions to precess at different frequencies and provides for spatial coding of the signal emitted from the body. The Larmor frequency at $\boldsymbol{x}$ is given by $w'(\boldsymbol{x}) = -\gamma(H_0 + \boldsymbol{G} \cdot \boldsymbol{x})$. Nuclei at specific positions or planes in the body may be excited selectively by applying RF pulses of specific frequencies. The combination of the gradient fields and the RF pulses applied is called the pulse sequence.
- An *RF detector system* to detect the RF signals emitted from the body. The RF signal measured outside the body represents the sum of the RF signals emitted by active nuclei from a certain part or slice of the body, as determined by the pulse sequence. The spectral spread of the RF signal provides information on the location of the corresponding source nuclei.
- A *computing and imaging system* to reconstruct images from the measured data, as well as process and display the images. Depending on the pulse sequence applied, the RF signal sensed may be formulated as the 2-D or 3-D *FT* of the image to be reconstructed (28, 33, 39). The data measured correspond to samples of the 2-D *FT* of a sectional image at points on concentric squares or circles (28). The Fourier or backprojection methods described in the preceding sections may then be used to obtain the image.

The image obtained is a function of the nuclear spin density in space and the corresponding parameters of the relaxation processes involved.
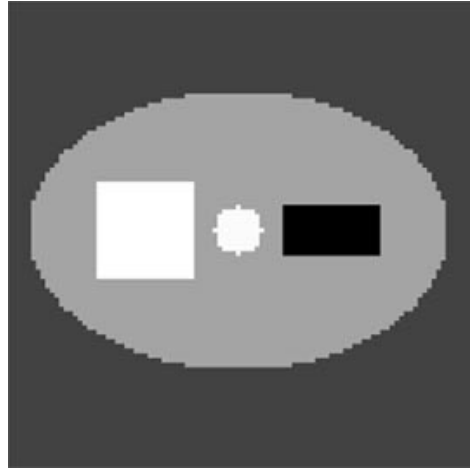
Fig. 9.   A synthetic 2-D image (phantom) with 101×101 8-bit pixels, representing a cross section of a 3-D object.

Examples of Reconstructed Images

Figure 9 shows a synthetic 2-D image (phantom), which we will consider to represent a cross section of a 3-D object. The objects in the image were defined on a discrete grid and hence have step and/or jagged edges. Figure 10(a) is a plot of the projection of the phantom image computed at 90°; note that the values are all positive. Figure 10(b) is a plot of the filtered projection using only the ramp filter ($|w|$) required in the *FBP* algorithm; note that the filtered projection has negative values.

Figure 11 shows the reconstruction of the phantom obtained using 90 projections from 2° to 180° in steps of 2° with the simple *BP* algorithm. While the objects in the image are visible, the smearing effect of the *BP* algorithm is obvious. Figure 12 shows the reconstruction of the phantom obtained using 90 projections with the *FBP* algorithm; only the ramp cfilter essential for the *FBP* process was used with no other smoothing or lowpass filter function. The contrast and visibility of the objects are better than those in the case of the simple *BP* result; however, the image is noisy due to the increasing gain of the ramp filter at higher frequencies. The reconstructed image also exhibits artifacts related to computation of the projections on a discrete grid; please refer to 18, 36, and 12 for discussions on this topic. The use of additional filters could reduce the noise and artifacts: Fig. 13 shows the result of reconstruction with the *FBP* algorithm including a fourth-order Butterworth filter with the 3 dB cutoff at 0.2 times the sampling frequency. The Butterworth filter has suppressed the noise and artifacts at the expense of blurring the edges of the objects in the image.

Figure 14 shows the reconstruction of the phantom obtained using 90 projections with three iterations of ART, as in Eq. (8). Projections for use with *ART* were computed from the phantom image data using an angle-dependent ray width, given by max ($|\sin \theta|$, $|\cos \theta|$) (19, 40). The quality of the reconstruction is better than that given by the *BP* or *FBP* algorithms.

The Radon transform may be interpreted as a transformation of the given image from the (x, y) space to the (t, θ) space. In practical *CT* scanning, the projection or ray integral data are obtained as samples at discrete intervals in t and θ. Just as we encounter the (Nyquist or Shannon) sampling theorem in the representation of a 1-D signal in terms of its samples in time, we now encounter the requirement to sample adequately along both the t and θ axes. A major distinction lies in the fact that the measurements made are discrete to begin with, and the signal (the body or object being imaged) cannot be prefiltered to prevent aliasing. Undersampling in either axis will lead to aliasing errors and poor reconstructed images. Figures 15, 16, and 17 show reconstructed
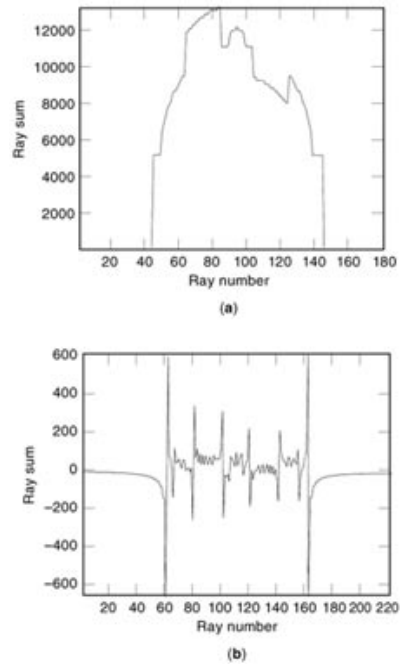
Fig. 10. (a) Projection of the phantom image in Fig. 9 computed at 90°. (b) Filtered version of the projection using only the ramp filter required in the *FBP* algorithm.
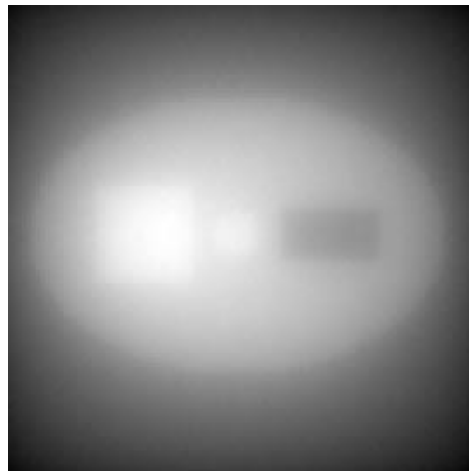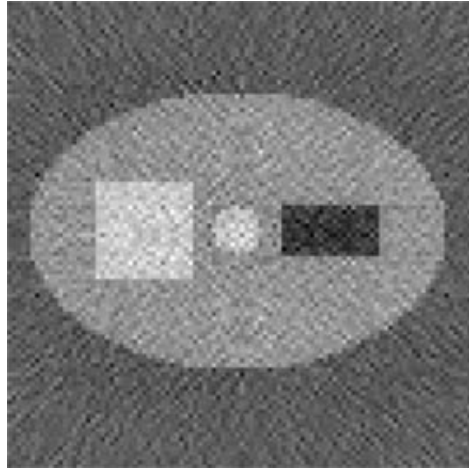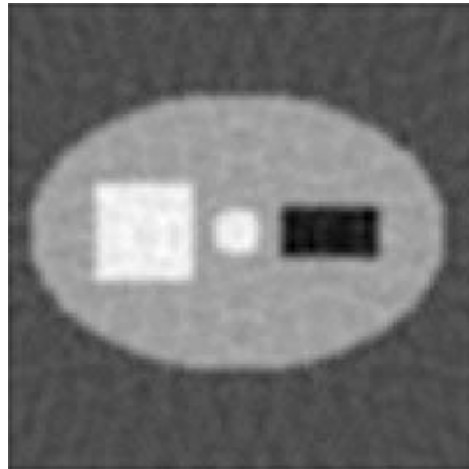

Fig. 11. Reconstruction of the phantom in Fig. 9 obtained using 90 projections from 2° to 180° in steps of 2° with the simple *BP* algorithm.

images obtained using only 10 projections spanning the 0° to 180° range in sampling steps of 18° and using the BP, FBP, and *ART* algorithms, respectively. The advantage of *ART* due to the use of the positivity constraint (*a priori* knowledge imposed) and the ability to iterate is seen in the improved quality of the result.

Fig. 12.   Reconstruction of the phantom in Fig. 9 obtained using 90 projections from 2° to 180° in steps of 2° with the *FBP* algorithm; only the ramp filter essential for the *FBP* process was used.

Fig. 13.   Reconstruction of the phantom in Fig. 9 obtained using 90 projections from 2° to 180° in steps of 2° with the *FBP* algorithm; the ramp filter essential for the *FBP* process was used along with a Butterworth lowpass filter.

Figures 18,19, and 20 show reconstructed images obtained using 10 projections but spanning only the angular range of 40° to 130° in steps of 10°. The limited angular coverage provided by the projections has clearly affected the quality of the image. Again, *ART* has provided the best possible reconstruction among the algorithms used in the study.

The use of limited projection data in reconstruction results in geometric distortion and streaking artifacts. The distortion may be modeled by the *PSF* of the reconstruction process (if it is linear and shift invariant, as BP, FBP, and unconstrained *ART* are). The PSFs of the simple *BP* method are shown as images in Fig. 21, for the case with 10 projections over 180°, and in Fig. 22, for the case with 10 projections from 40° to 130°. The reconstructed image is given by the convolution of the original (unknown) image with the PSF. Limited
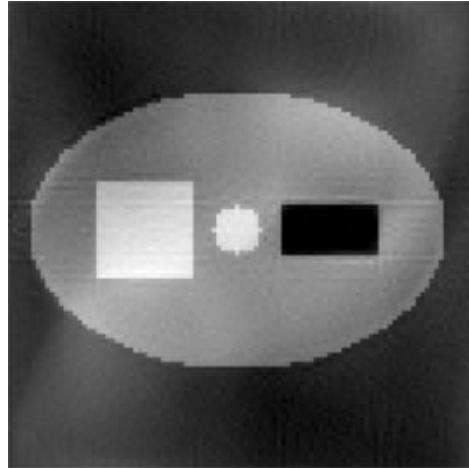
Fig. 14.   Reconstruction of the phantom in Fig. 9 obtained using 90 projections from 2° to 180° in steps of 2° with three iterations of constrained additive ART.
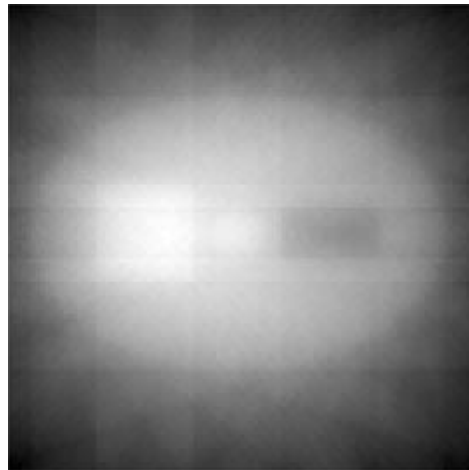

Fig. 15.   Reconstruction of the phantom in Fig. 9 obtained using 10 projections from 18° to 180° in steps of 18° with the simple *BP* algorithm.

improvement in image quality may be obtained by applying deconvolution filters to the reconstructed image (41424344454647–48).

Display of ct Images

X-ray *CT* is capable of producing images with very good density resolution, on the order of 1 part in 1000. For display purposes, the attenuation coefficients are normalized with respect to that of water and expressed as $H = 1000(\mu/\mu_w - 1)$ Hounsfield units, where μ is the measured attenuation coefficient, and μ_w is the attenuation coefficient of water. The *CT* number is expressed in Hounsfield units, named after the inventor of the first
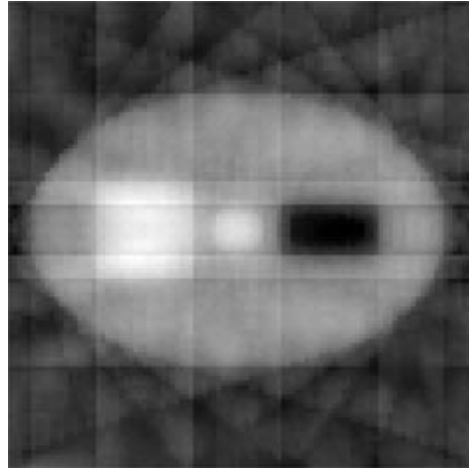
Fig. 16. Reconstruction of the phantom in Fig. 9 obtained using 10 projections from 18° to 180° in steps of 18° with the *FBP* algorithm; the ramp filter essential for the *FBP* process was used along with a Butterworth lowpass filter.
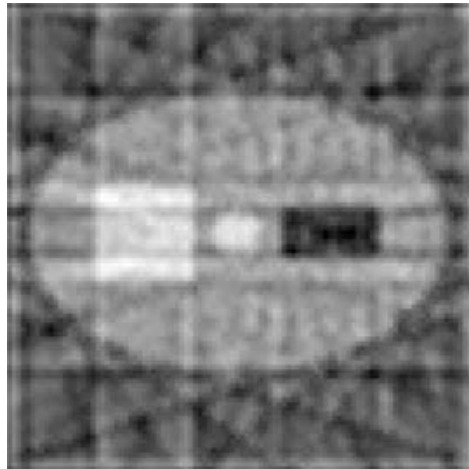

Fig. 17. Reconstruction of the phantom in Fig. 9 obtained using 10 projections from 18° to 180° in steps of 18° with three iterations of constrained additive ART.

commercial medical *CT* scanner (10). This scale results in values of about $+1000$ for bone, 0 for water, about -1000 for air, 20 to 80 for soft tissue, and about -800 for lung tissue (22).

The dynamic range of *CT* values is much wider than those of common display devices and the human visual system at a given level of adaptation. Furthermore, detailed diagnosis requires visualization of small density differences. For these reasons, presentation of the entire range of values available in a *CT* image in a single display is neither practically feasible nor desirable. In practice, small "windows" of the *CT* number scale are chosen and linearly expanded to occupy the capacity of the display device. The window width and level (center) values may be chosen interactively to display different density ranges with improved perceptibility of details within the chosen density window. (Values above or below the window limits are displayed as totally
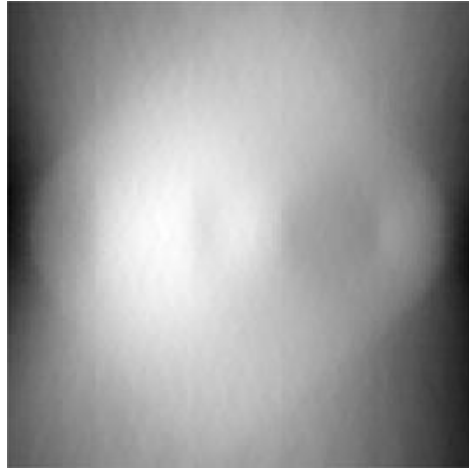
Fig. 18.   Reconstruction of the phantom in Fig. 9 obtained using 10 projections from 40° to 130° in steps of 10° with the simple *BP* algorithm.
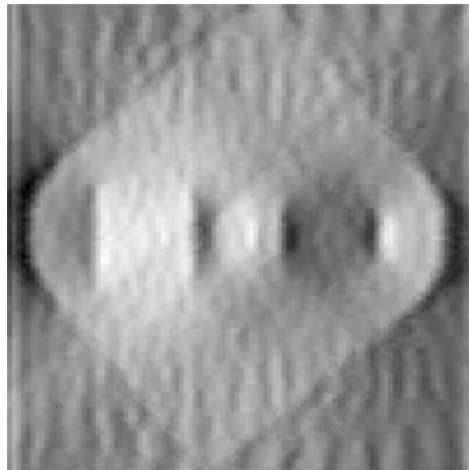

Fig. 19.   Reconstruction of the phantom in Fig. 9 obtained using 10 projections from 40° to 130° in steps of 10° with the *FBP* algorithm; the ramp filter essential for the *FBP* process was used along with a Butterworth low-pass filter.

white or black, respectively.) This technique, known as windowing or density slicing, may be expressed as

$$g(x, y) = \frac{f(x, y) - m}{M - m} (N - n) + n$$

where $f(x, y)$ is the original image in *CT* numbers, $g(x, y)$ is the windowed image to be displayed, (m, M) is the range of *CT* values in the window to be displayed, and (n, N) is the range of the display values. The window width is $(M - m)$ and the window level is $(M + m)/2$; the display range is typically $n = 0$ and $N = 255$ with 8 bit display systems. Figure 23 shows a set of two *CT* images of a patient with head injury, with each image displayed with two sets of window level and width. The effects of the density window chosen on the features
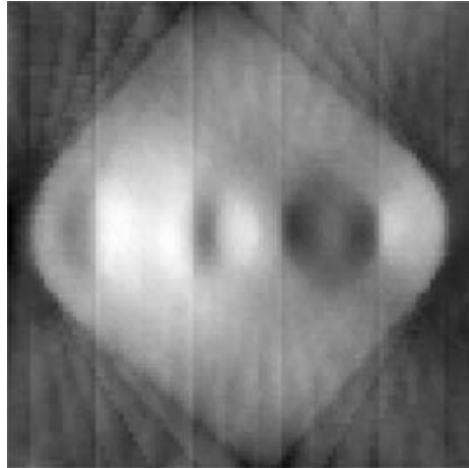
Fig. 20.   Reconstruction of the phantom in Fig. 9 obtained using 10 projections from 40° to 130° in steps of 10° with three iterations of constrained additive ART.
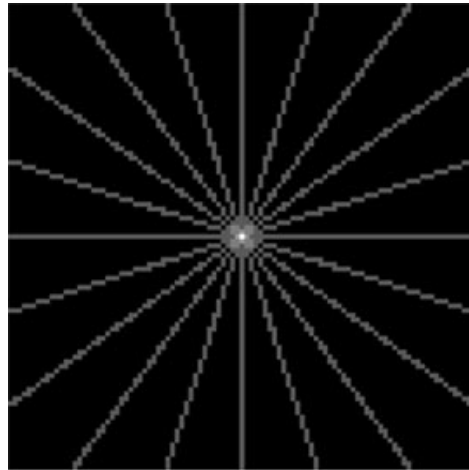

Fig. 21.   Point spread function of the simple *BP* procedure using 10 projections spread evenly over 180°.

of the image displayed are clearly seen in the figure: either the fractured bone or the brain matter are seen in detail in the windowed images, but not both in the same image.

A dramatic visualization of details may be achieved by pseudocolor techniques. Arbitrary or structured color scales could be assigned to *CT* values by look-up tables or gray-scale-to-color transformations. Some of the popular color transforms are the rainbow (*VIBGYOR*) and the heated metal color (red–yellow–white) sequences. Difficulties may arise, however, in associating density values with different colors if the transformation is arbitrary and not monotonic in intensity or total brightness. A look-up table linking the displayed colors to *CT* numbers or other pixel attributes may assist in improved visual analysis of image features in engineering and scientific applications.
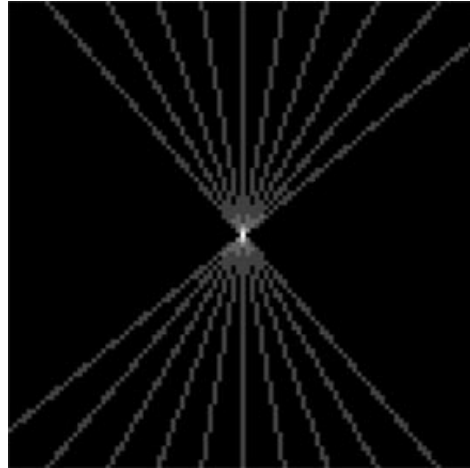
Fig. 22.   Point spread function of the simple *BP* procedure using 10 projections from 40° to 130° in steps of 10°.
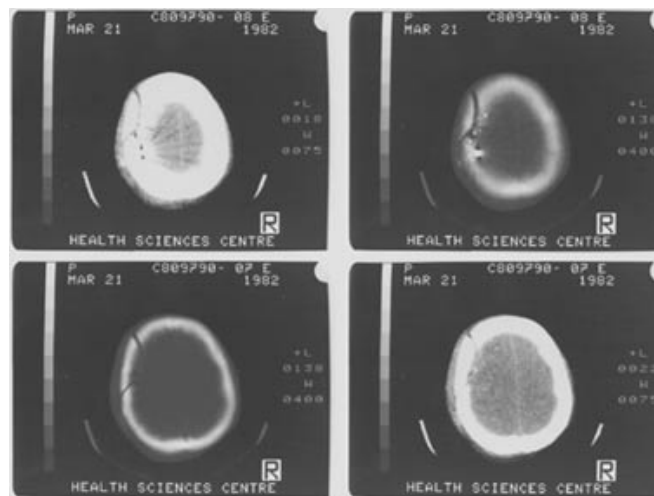

Fig. 23.   A set of two *CT* images of a patient with head injury, with each image displayed with two sets of window level and width. One of the windows displays the skull, the fracture, and the bone segments, but the brain matter is not visible; the other window displays the brain matter in detail, but the fracture area is saturated. (Courtesy of Dr. W. Gordon, Health Sciences Centre, Winnipeg, MB, Canada.)

Industrial Applications

The phenomenal success of *CT* in diagnostic medicine attracted interest from many other disciplines in recent years (4950515253545556–57). The petroleum industry has demonstrated significant interest, with the objective of determining physical properties of porous rocks and fluid saturations during multiphase flow phenomena associated with petroleum and natural gas production (49, 50, 52). Most major oil companies possess some form of an in-house *CT* system, although a considerable number of exploratory projects have been performed in hospitals after patient-imaging hours. Recently, the term "process tomography" has been identified with the development and use of tomographic imaging techniques for industrial applications (51, 53). The
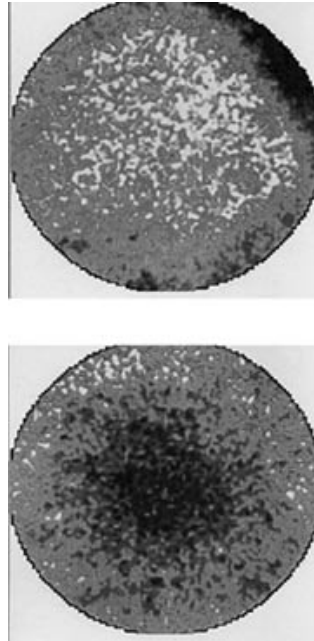
Fig. 24.   X-ray *CT* images of multiphase flow in porous media.

possibility of identifying elements of different density and/or different atomic number within a study sample gives a wide potential for industrial applications, some of which are described in the following paragraphs.

The characterization of cores from oil and gas reservoirs using *CT* is based on the following principles. The normalized X-ray attenuation numbers of a *CT* image are proportional to the bulk density of the sample under study for the energies at which commercial medical X-ray *CT* scanners operate (49, 50). The atomic number effect in samples consisting of elements of atomic number up to 20 is negligible. A linear relationship between *CT* number and bulk density can be established through a simple calibration process. In reservoir rock characterization studies, density variations can be translated into porosity maps and specific feature maps (such as vugs and fractures). Density contrast can also be used to identify the distribution of up to two fluids within reservoir rocks, such as oil/water, oil/gas, or water/gas (50, 52). However, the density contrast is often not enough to show quantitative fluid saturation distribution. Contrast enhancement may be achieved by "doping" one of the fluid phases with a high-contrast agent (such as iodide salts). Several attempts have been made to quantify three-phase saturation distribution through selected doping agents and dual-energy scanning, but with limited success (58).

Figure 24 shows a typical example of the application of X-ray *CT* in reservoir rock characterization. The first image shows a typical cross section of a relatively uniform sand pack that contains water. The second image shows the same cross section after a polymer solution was injected into the sand pack; the image clearly identifies the area in which the solution has displaced oil and water.

59 developed a portable X-ray and gamma-ray minitomograph for application in soil science; in particular, they used the scanner to measure water content and bulk density of soil samples. Soil-related studies may address identification of features (such as fractures, wormholes, and roots) and flow of various contaminants in soil. Some exotic applications have also appeared in the literature, such as the use of *CT* to determine the quality of turf in golf courses.

Recently, numerous applications of *CT* have appeared in projects related to monitoring of multiphase flow phenomena in pipes and in models of chemical reactors (53, 54). In these cases, the objective is to determine flow phenomena associated with modeling of specific chemical reactor problems. Pipe-flow studies were published first, and fluidized-bed problems and trickle-bed problems began appearing in the literature in the 1990s. In many of the chemical reactor problems studied via CT, new custom-made *CT* systems have been described in the literature, such as gamma-ray *CT* devices and a variety of electrical *CT* systems that utilize capacitance, resistivity, or impedance variability in the systems under study (51, 53).

Forestry applications of *CT* have appeared in the literature in the form of scanning of live trees to measure growth rings and detect decay using a portable X-ray *CT* scanner (60), and monitoring tree trunks or logs in the timber industry.

Applications of *CT* for characterization of other materials has had limited success. Studies on polymer characterization have shown that *CT* can be used to study structural defects and other heterogeneities in polymer objects (61). Algorithms for material characterization based on atomic number differences have also been presented in the literature; multiple-energy imaging has been used for such studies. Imaging of steel objects has been performed with high-energy gamma-ray scanners for studies on structural failure and corrosion (62). *CT* scanners have been custom-built for inspection of turbine engines and rocket boosters.

The resolution of *CT* devices used in industrial applications can vary significantly, reaching down to 200 μm by 200 μm pixels in cross section. Special systems have been built to image small samples (less than 1 cm^3 in volume) with resolutions of about 5 μm by 5 μm in cross section (63, 64). Such an imaging procedure is called microtomography, being a hybrid of tomography and microscopy. Most microtomography studies are performed with finely focused radiation beams produced by a particle accelerator. Porous media studies (63) and polymer characterization studies (64) have been reported using microtomography.

Application of *CT* imaging in geotechnical engineering is promising. Published examples of geotechnical *CT* imaging include pipeline–soil interactions, modeling of tectonic plate movements, and determining stress–strain relationships and stress effects in various media (65).

Industrial applications of *SPECT* have been limited in scope. The major application of *SPECT* in chemical engineering is for real-time tracer work and radioactive particle tracking. Radio-pharmaceuticals are used to tag either a fluid phase or a solid particle and to follow the trajectories in real time. Applications include flow in porous media and fixed-bed reactors. Radioactive particle tracking has also been used to monitor solid flow in fluidized beds and solid handling systems (66).

Figure 25 shows an example of a solid circulation map in a laboratory fluidized-bed column. The map is depicted as a probability density function of a given particle being at a location in the column. Maps such the one in Fig. 25 can be used for modeling flow phenomena in fluidized-bed reactors.

Figure 26 shows two sets of *MR* images of samples of a sandstone reservoir (67). Longitudinal and transversal images are shown for each sample. The core at the top is a layered sandstone sample: distinct bedding planes are visible. The sample at the bottom exhibits large pores as bright spots.

Concluding Remarks

The 1980s and 1990s have brought out many new developments in *CT* imaging. Continuing development of versatile imaging equipment and image processing algorithms has been opening up newer applications of *CT* imaging. Three-dimensional imaging of moving organs such as the heart is now feasible. Three-dimensional display systems and algorithms have been developed to provide new and intriguing displays of the interior of the human body. Three-dimensional images obtained by *CT* are being used in surgery and radiation therapy, creating the new fields of image-guided surgery and treatment. Practical realization of portable scanners has also made possible field applications in agricultural sciences and other areas. *CT* is a truly revolutionary investigative imaging technique—a remarkable synthesis of many scientific principles.
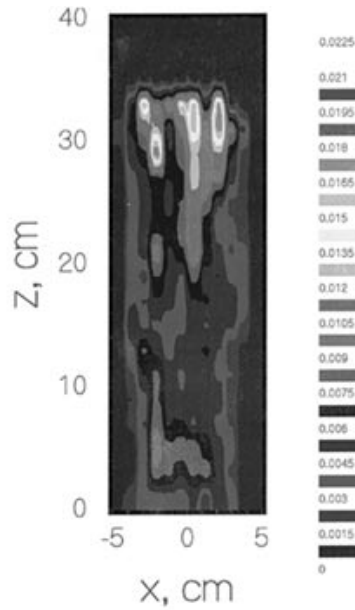
Fig. 25.   Probability density function of the position of a solid particle in a fluidized-bed obtained by *SPECT* imaging.
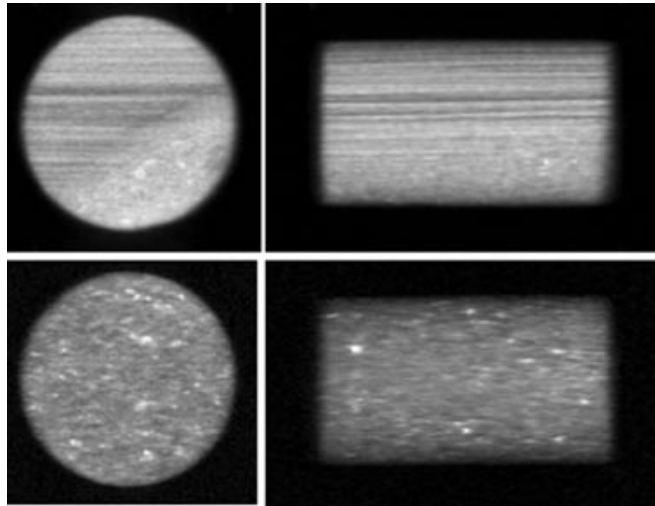

Fig. 26.   *MR* images of reservoir cores obtained by using a Bruker Biospec *MR* scanner operating at 2.35 T and 100 MHz. Top: layered sandstone; bottom: sandstone with fairly large pores. Bright areas correspond to high proton concentration.

Acknowledgments

BIBLIOGRAPHY

1. J. Radon, Über die Bestimmung von Funktionen durch ihre Integralwerte längs gewisser Mannigfaltigkeiten, *Math. Phys. K.*, **69**: 262, 1917.

2. A. M. Cormack, Representation of a function by its line integrals, with some radiological applications, *J. Appl. Phys.*, **34**: 2722–2727, 1963.

3. A. M. Cormack, Representation of a function by its line integrals, with some radiological applications II, *J. Appl. Phys.*, **35**: 2908–2913, 1964.

4. R. N. Bracewell A. C. Riddle, Inversion of fan-beam scans in radio astronomy, *Astrophys. J.*, **150**: 427–434, 1967.

5. R. A. Crowther, *et al.* Three dimensional reconstructions of spherical viruses by Fourier synthesis from electron micrographs, *Nature*, **226**: 421–425, 1970.

6. D. J. De Rosier A. Klug, Reconstruction of three dimensional images from electron micrographs, *Nature*, **217**: 130–134, 1968.

7. G. N. Ramachandran A. V. Lakshminarayanan, Three-dimensional reconstruction from radiographs and electron micrographs: Application of convolutions instead of Fourier transforms, *Proc. Natl. Acad. Sci. USA*, **68**: 2236–2240, 1971.

8. R. Gordon, R. Bender, G. T. Herman, Algebraic reconstruction techniques (*ART*) for three-dimensional electron microscopy, *J. Theor. Biol.*, **29**: 471–481, 1970.

9. W. H. Oldendorf, Isolated flying spot detection of radio-density discontinuities displaying the internal structural pattern of a complex object, *IRE Trans. Bio-Med. Elect.*, **BME-8**: 68, 1961.

10. G. N. Hounsfield, Computerized transverse axial scanning (tomography): Part 1. Description of system, *Br. J. Radiol.*, **46**: 1016–1022, 1973.

11. J. Ambrose, Computerized transverse axial scanning (tomography): Part 2. Clinical application, *Br. J. Radiol.*, **46**: 1023–1047, 1973.

12. A. C. Kak M. Slaney, *Principles of Computerized Tomographic Imaging*, Piscataway, NJ: IEEE Press, 1988.

13. A. Rosenfeld A. C. Kak, *Digital Picture Processing*, 2nd ed., New York: Academic Press, 1982.

14. A. K. Louis F. Natterer, Mathematical problems of computerized tomography, *Proc. IEEE*, **71**: 379–389, 1983.

15. R. M. Lewitt, Reconstruction algorithms: Transform methods, *Proc. IEEE*, **71**: 390–408, 1983.

16. Y. Censor, Finite series-expansion reconstruction methods, *Proc. IEEE*, **71**: 409–419, 1983.

17. G. T. Herman, *Image Reconstruction from Projections: Implementation and Applications*, Berlin: Springer-Verlag, 1979.

18. G. T. Herman, *Image Reconstruction from Projections: The Fundamentals of Computed Tomography*, New York: Academic Press, 1980.

19. R. Gordon, A tutorial on *ART* (algebraic reconstruction techniques), *IEEE Trans. Nucl. Sci.*, **21**: 78–93, 1974.

20. R. Gordon G. T. Herman, Three-dimensional reconstruction from projections: A review of algorithms, *Int. Rev. Cytol.*, **38**: 111–151, 1974.

21. P. Edholm, The tomogram—its formation and content. *Acta Radiol.*, Suppl. No. **193**: 1–109, 1960.

22. R. A. Robb, X-ray computed tomography: An engineering synthesis of multiscientific principles, *CRC Crit. Rev. Biomed. Eng.*, **7**: 264–333, 1982.

23. R. M. Rangayyan, Computed tomography techniques and algorithms: A tutorial, *Innovation Technol. Biol. Med.*, **7** (6): 745–762, 1986.

24. D. P. Boyd, *et al.* Proposed dynamic cardiac 3-D densitometer for early detection and evaluation of heart disease, *IEEE Trans. Nucl. Sci.*, **NS-26**: 2724–2727, 1979.

25. D. P. Boyd M. J. Lipton, Cardiac computed tomography, *Proc. IEEE*, **71**: 298–307, 1983.

26. R. A. Robb, *et al.* High-speed three-dimensional x-ray computed tomography: The Dynamic Spatial Reconstructor, *Proc. IEEE*, **71**: 308–319, 1983.

27. S. A. Larsson, Gamma camera emission tomography, *Acta Radiol. Suppl.*, 363, 1980.

28. Z. H. Cho, J. P. Jones, M. Singh, *Foundations of Medical Imaging*, New York: Wiley, 1993.

29. A. Macovski, *Medical Imaging Systems*, Englewood Cliffs, NJ: Prentice-Hall, 1983.

30. G. F. Knoll, Single-photon emission computed tomography, *Proc. IEEE*, **71**: 320–329, 1983.

31. A. Macovski, Physical problems of computerized tomography, *Proc. IEEE*, **71**: 373–378, 1983.

32. J. F. Greenleaf, Computerized tomography with ultrasound, *Proc. IEEE*, **71**: 330–337, 1983.

33. W. S. Hinshaw A. H. Lent, An introduction to *NMR* imaging: From the Bloch equation to the imaging equation, *Proc. IEEE*, **71**: 338–350, 1983.

34. G. Müller *et al.*(eds.), *Medical Optical Tomography: Functional Imaging and Monitoring*, Bellingham, WA: SPIE Optical Engineering Press, 1993.

35. H. Guan R. Gordon, Computed tomography using *ART* with different projection access schemes: A comparison study under practical situations, *Phys. Med. Biol.*, **41**: 1727–1743, 1996.

36. G. T. Herman, A. Lent, S. W. Rowland, ART: Mathematics and applications—a report on the mathematical foundations and on the applicability to real data of the algebraic reconstruction techniques, *J. Theor. Biol.*, **42**: 1–32, 1973.

37. A. Lent, A convergent algorithm for maximum entropy image restoration, with a medical x-ray application, in R. Shaw (ed.), *Image Analysis and Evaluation*, Washington, DC: Society of Photographic Scientists and Engineers, 1977, pp. 249–257.

38. P. Gilbert, Iterative methods for the three-dimensional reconstruction of an object from projections, *J. Theor. Biol.*, **36**: 105–117, 1972.

39. P. C. Lauterbur C. M. Lai, Zeugmatography by reconstruction   from projections, *IEEE Trans. Nucl. Sci.*, **27**: 1227–1231, 1980.

40. R. M. Rangayyan R. Gordon, Streak preventive image reconstruction via *ART* and adaptive filtering, *IEEE Trans. Med. Imaging*, **1**: 173–178, 1982.

41. R. Gordon R. M. Rangayyan, Geometric deconvolution: A meta-algorithm for limited view computed tomography, *IEEE Trans. Biomed. Eng.*, **30**: 806–810, 1983.

42. R. Gordon, A. P. Dhawan, R. M. Rangayyan, Reply to comments on geometric deconvolution: A meta-algorithm for limited view computed tomography, *IEEE Trans. Biomed. Eng.*, **32**: 242–244, 1985.

43. P. J. Soble, R. M. Rangayyan, R. Gordon, Quantitative and qualitative evaluation of geometric deconvolution of distortion in limited-view computed tomography, *IEEE Trans. Biomed. Eng.*, **32**: 330–335, 1985.

44. R. M. Rangayyan, R. Gordon, A. P. Dhawan, Algorithms for limited-view computed tomography: An annotated bibliography and a challenge, *Appl. Opt.*, **24** (23): 4000–4012, 1985.

45. A. P. Dhawan, R. M. Rangayyan, R. Gordon, Image restoration by Wiener deconvolution in limited-view computed tomography, *Appl. Opt.*, **24** (23): 4013–4020, 1985.

46. D. Boulfelfel, *et al.* Three-dimensional restoration of single photon emission computed tomography images, *IEEE Trans. Nucl. Sci.*, **41**: 1746–1754, 1994.

47. D. Boulfelfel, *et al.* Restoration of single photon emission computed tomography images by the Kalman filter, *IEEE Trans. Med. Imaging*, **13**: 102–109, 1994.

48. D. Boulfelfel, *et al.* Pre-reconstruction restoration of single photon emission computed tomography images, *IEEE Trans. Med. Imaging*, **11**: 336–341, 1992.

49. A. Kantzas, Investigation of physical properties of porous rocks and fluid flow phenomena in porous media using computer assisted tomography, *In Situ*, **14** (1): 77–132, 1990.

50. A. Kantzas, D. F. Marentette, K. N. Jha, Computer assisted tomography: From qualitative visualization to quantitative core analysis, *J. Can. Petrol. Tech.*, **31** (9): 48–56, 1992.

51. R. A. Williams M. S. Beck, *Process Tomography; Principles, Techniques and Applications*, London: Butterworth Heinemann, 1995.

52. S. L. Wellington H. J. Vinegar, X-ray computerized tomography, *J. Petrol. Technol.*, **39** (8): 885–898, 1987.

53. D. M. Scott R. A. Williams, *Frontiers in Industrial Process Tomography*, Proc. Eng. Found. Conf., The Cliffs Shell Beach, CA, 1995.

54. J. Chaouki, F. Larachi, M. P. Duduković (ed.), *Non-invasive Monitoring of Multiphase Flows*, Amsterdam: Elsevier, 1997.

55. J. L. Ackerman W. A. Ellingson (eds.), *Advanced Tomographic Imaging Methods for the Analysis of Materials*, Pittsburgh, PA: Materials Research Society, 1991.

56. *Technical Digest of the Topical Meeting on Industrial Applications of Computed Tomography and NMR Imaging*, Optical Society of America, Hecla Island, Manitoba, Canada, 1984.

57. Special Issue. Collection of papers from the Optical Society of America Topical Meeting on Industrial Applications of Computed Tomography and NMR Imaging, *Appl. Opt.*, **24** (23): 3948–4133, 1985.

58. A. Kantzas, Applications of computer assisted tomography in the quantitative characterization of porous rocks, *Int. Symp. Soc. Core Analysts—CT Workshop*, Stavanger, Norway, Sept. 1994.

59. P. E. Cruvinel, *et al.* X- and gamma-rays computerized minitomograph scanner for soil science, *IEEE Trans. Instrum. Meas.*, **39**: 745–750, 1990.

60. A. M. Onoe, *et al.* Computed tomography for measuring annual rings of a live tree, *Proc. IEEE*, **71**: 907–908, 1983.

61. S. Persson E. Ostman, Use of computed tomography in non-destructive testing of polymeric materials, *Appl. Opt.*, **24** (23): 4095, 1985.

62. B. D. Sawicka R. L. Tapping, CAT scanning of hydrogen induced cracks in steel, *Nucl. Instrum. Methods Phys. Res. A*, **256**: 103, 1987.

63. M. E. Coles, *et al.* Developments in synchrotron x-ray microtomography with applications to flow in porous media, *SPE Reservoir Eval. Eng.*, **1** (4): 288–296, 1998.

64. W. C. Conner, *et al.* Use of x-ray microscopy and synchrotron microtomography to characterize polyethylene polymerization particles, *Macromolecules*, **23** (22): 4742–4747, 1990.

65. A. Kantzas, Stress–strain characterization of sand packs under uniform loads as determined from computer-assisted tomography, *J. Can. Petrol. Technol.*, **36** (6): 48–52, 1997.

66. A. Kantzas, *et al.* Application of gamma camera imaging and *SPECT* systems in chemical processes, *First World Congress on Industrial Process Tomography*, Buxton, Greater Manchester, UK, Apr. 1999.

67. K. Mirotchnik, *et al.* Determination of mud invasion characteristics of sandstone reservoirs using a combination of advanced core analysis techniques, *Proc. 1998 Int. Symp. Soc. Core Analysts*, The Hague, The Netherlands, Sept. 1998, p. SCA9815.

RANGARAJ M. RANGAYYAN
APOSTOLOS KANTZAS
University of Calgary